J. Fluid Mech. (2011), *vol.* 668, *pp.* 33–57.
doi:10.1017/S0022112010004519

Three-dimensional features in low-Reynolds-number confined corner flows

LAURA GUGLIELMINI[1]†, R. RUSCONI[2], S. LECUYER[2] AND H.A. STONE[1]

[1]Department of Mechanical and Aerospace Engineering, Princeton University, Princeton, NJ 08544, USA
[2]School of Engineering and Applied Sciences, Harvard University, Cambridge, MA 02138, USA

(Received 26 March 2010; revised 19 August 2010; accepted 23 August 2010;
first published online 13 December 2010)

In recent microfluidic experiments with solutions of bacteria we observed the formation of biofilms in the form of thread-like structures, called 'streamers', which float in the middle plane of the channel and are connected to the side walls at the inner corners. Motivated by this observation, we discuss here the pressure-driven low-Reynolds-number flow around a corner bounded by the walls of a channel with rectangular cross-section. We numerically solve the flow field in a channel of constant cross-section, which exhibits 90° sharp corners, or turns with constant curvature, or portions with slowly changing curvature along the flow direction, for finite, but small, values of the Reynolds numbers and including the limit of vanishingly small Reynolds numbers. In addition, we develop a matched asymptotic expansion solution for the flow around two boundaries intersecting at an angle α and spanning the small gap h between two horizontal plates. We illustrate the basic features of the flow in these channel geometries by describing the three-dimensional velocity field and the distribution of streamwise vorticity and helicity, and comparing the numerical solutions with predictions based on the asymptotic approach. We demonstrate that near a corner or a change in the curvature of the side wall the flow is three-dimensional and pairs of counter-rotating vortical structures are present, as identified by Balsa (*J. Fluid Mech.*, vol. 372, 1998, p. 25). Finally, we discuss how this secondary flow depends on the significant geometric parameters, the aspect ratio of the channel cross-section, the radius of curvature of the turn and, more generally, the variation of the curvature of the channel side boundary. We believe that these three-dimensional secondary flow structures are relevant to transport problems where accumulation of material at the boundary is possible.

Key words: Hele-Shaw flows, microfluidics, Stokesian dynamics

1. Introduction

Two-dimensional low-Reynolds-number corner flows are well characterized and described in textbooks. If the corner angle is small enough, sufficiently close to the corner, such flows are characterized by an infinite sequence of progressively weaker, closed eddies, while for larger angles they have open streamlines (Moffatt 1964;

† Email address for correspondence: lauragug@stanford.edu, hastone@princeton.edu

Davis & O'Neill 1977; Jeffrey & Sherwood 1980). Much less is known about three-dimensional corner flows, though over the past 10 years a number of studies have been devoted to the description of such flows. All of these studies have considered boundary-driven motions and have identified conditions where closed eddies are generated (Hills & Moffatt 2000; Shankar 2000, 2007; Gomilko, Malyuga & Meleshko 2003). In this paper, motivated by recent experiments, we consider pressure-driven flow around three-dimensional corners using both numerical and analytical methods.

The field of microfluidics has generated many new studies of fluid dynamics problems (Stone, Stroock & Ajdari 2004; Squires & Quake 2005). With reference to the present study we note that, while in the most simple microfluidic designs the channels are straight, curves and corners are introduced whenever there is the need to produce long channels in a finite space. More generally, in channel flows and in all kinds of fluid-handling processes, corners and bends are common features. Some generic features of the low-Reynolds-number flow in such geometries are known. Balsa (1998) examined the low-Reynolds-number fluid motion around a cylindrical object that spans the gap of a Hele-Shaw cell and showed that the region adjacent to the object contains secondary streamwise vorticity as the result of a variation of the curvature of the side boundary. In fact, this problem was first identified by Riegels (1938) and solved by Thompson (1968) using the method of matched asymptotic expansion. These calculations identify the three-dimensional nature of the flow in a Hele-Shaw geometry near a transverse boundary that induces variations in the curvature of flow streamlines; see also the three-dimensional eigenfunction solution presented by Lee & Fung (1969). In addition, it has been shown that, in a pressure-driven laminar channel flow, if the centreline does not have a constant curvature, or if the shape of the channel cross-section varies along the flow direction, then the flow is necessarily three-dimensional (Lauga, Stroock & Stone 2004). In particular, Lauga *et al.* (2004) determined the most significant features of the flow field in a slowly varying sinusoidal channel. Also, a number of studies (Liu *et al.* 2000; Yi & Bau 2003) focused on moderate Reynolds number flows have investigated the possibility of exploiting the secondary vortical flow that appears in the proximity of a turn to achieve fluid mixing in channels that contain a sequence of 90° turns; some numerical details of the corner flow as a function of the Reynolds number were reported (Yi & Bau 2003). In this paper, we address, using simulations and analysis, detailed features of bounded laminar flows around an isolated corner at low-Reynolds number.

As motivation for our study, we briefly describe our recent experimental study of biofilm formation in channel flows (Rusconi *et al.* 2010). Biofilms are communities of bacterial cells held together in a self-secreted polymeric matrix. We studied how biofilms form when a bacterial solution flows through a typical microfluidic channel (figure 1*a*). In straight channels the biofilm formed, as expected, on the walls of the channel. To our surprise, we found that in microchannels with curves (typically the channel had a series of 90° turns) a biofilm, in the form of a suspended thread that slowly grew thicker in time, developed along the length of the channel, as shown in figure 1(*b*). The thread was connected to the side boundary downstream of each corner and was floating exactly in the middle plane of the channel, as illustrated in the three-dimensional confocal microscopy reconstructions in figure 1(*c*). These observations suggest an underlying connection between the fluid motion in the neighbourhood of the corner and the biological processes (cell adhesion to the boundaries, production of extracellular matrix) that eventually produce biofilm streamers. As we document in this paper, a viscous flow around a sharp corner generates vortical flow structures that plausibly reinforce the formation of polymeric aggregates that we have observed.

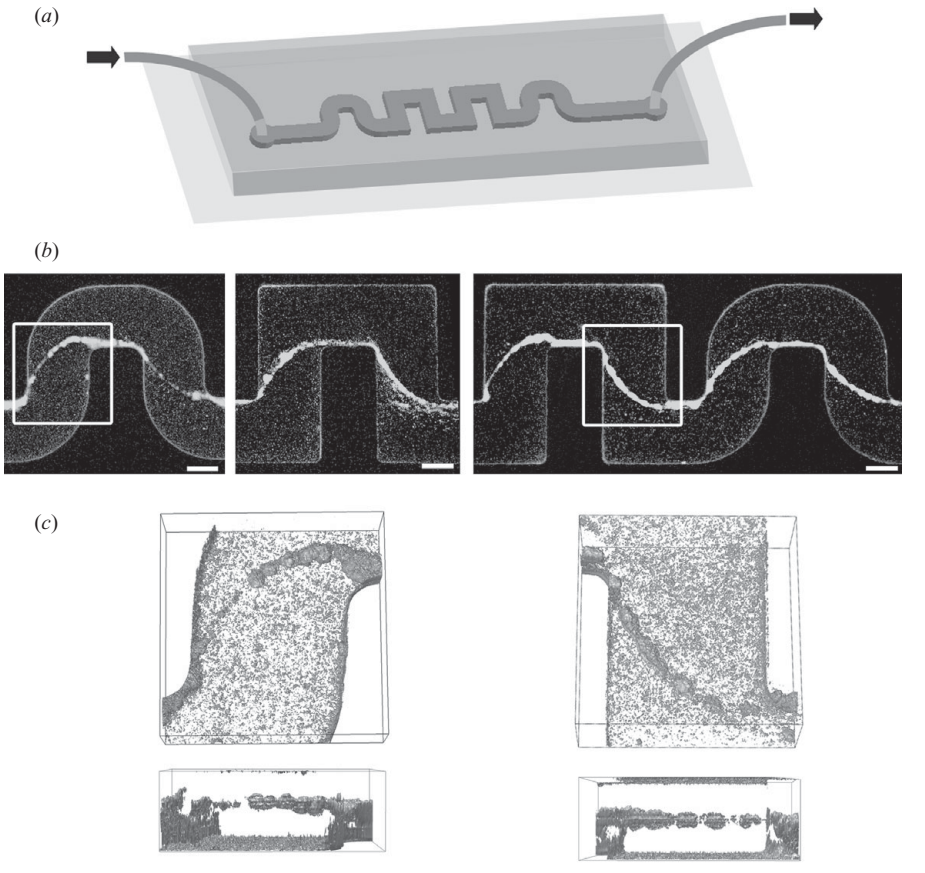

FIGURE 1. Experimental evidence for bacterial thread-like biofilms (streamers) in curved microchannels (Rusconi *et al.* 2010). (*a*) Schematic of the microfluidic device in which bacterial solutions, containing cells and nutrients, flow through the channel for several hours (not to scale). The width of the channel is 200 μm and the thickness is about 100 μm. (*b*) Bacterial streamers developed in the channels after 12 h at constant flow rate (corresponding to an average speed of 0.75 μl min^{-1}) for two different experiments. The flow direction is from left to right. Bacteria are fluorescently labelled, and images of the middle plane of the channel are taken with a confocal microscope. Scale bars, 100 μm. (*c*) Three-dimensional reconstruction of the streamers from confocal images. Two perspective and cross-sectional views are shown, corresponding to the positions highlighted by the boxes in (*b*).

We focus here on the underlying fluid dynamics problem and leave the description of the spatial and temporal evolution of a thread to a future study.

In § 2, we describe the numerical approach that we have used to study this problem. Next, in § 3 we illustrate the basic features of low-Reynolds-number flows in a three-dimensional confined geometry by describing the velocity field and the distribution of streamwise vorticity and helicity. In § 4, we introduce a matched asymptotic expansion solution for a flow around two boundaries that intersect at an angle α and span the small gap between two horizontal plates. Finally, in § 5, we discuss how the identified secondary flow depends on the geometric parameters, i.e. the aspect ratio of the channel cross-section, the radius of curvature of the turn and, more generally, the variation of the curvature of the side boundary of the channel. Numerical results are compared with the predictions of the asymptotic analysis.

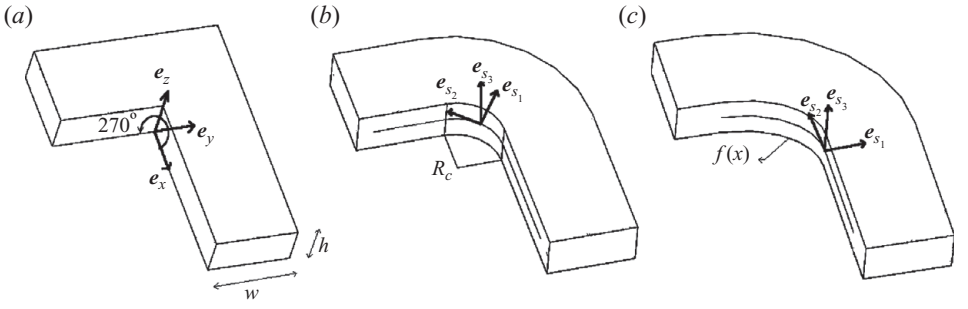

FIGURE 2. Schematic of the geometries discussed in this paper: a channel with rectangular cross-section which has (*a*) a 90° sharp corner turn, or (*b*) a 90° rounded turn with constant radius of curvature R_c, or (*c*) a generic continuous turn, where the position of one of the side boundaries is described by a function $f(x)$ of our choice. We introduce the Cartesian coordinate system (x, y, z), with x aligned with the axis of the inlet of the channel, and the orthogonal curvilinear coordinate system (s_1, s_2, s_3), with s_1 and s_2 lying in the middle plane of the channel and s_2 running along the inner sidewall.

2. Problem formulation

We consider a pressure-driven flow in a channel of constant rectangular cross-section, which exhibits a 90° turn that is characterized by either (i) a sharp corner, (ii) a corner of constant curvature or (iii) a corner with a slowly changing curvature along the flow direction (figure 2). We choose the x-direction to lie along the axis of the inlet of the channel, whose cross-section is characterized by a width w in the y-direction and a thickness h in the z-direction. The origin of the coordinate axis is located at the corner, on the bottom plane of the channel (see figure 2*a*). The radius of curvature of the turn for geometry (ii) is denoted R_c. We also introduce a curvilinear orthogonal coordinate system (s_1, s_2, s_3), centred on the plane of symmetry of the geometry (see figure 2*b*); for more general shapes, this coordinate system has its origin at the beginning of the curved section (see figure 2*c*), where s_1 and s_2 lie in the middle plane of the channel and s_2 runs along the inner sidewall of the channel. The flow is described by the Navier–Stokes and continuity equations and the problem formulation is completed by the no-slip boundary conditions at the four bounding surfaces. We note that in the geometry we mostly use (figure 2*a*), the two consecutive sidewalls that identify the inner corner intersect forming an angle of 270° in the fluid domain, which is to be contrasted with the studies of Shankar (2000) and Gomilko *et al.* (2003), who solved the boundary-driven Stokes flow in the wedge identified by three walls that intersect at 90° or smaller angles.

We non-dimensionalize the governing equations using half the channel width $w/2$ as the length scale and the average velocity in the channel section U as the velocity scale. The channel cross-section is then characterized by the ratio ϵ between the channel thickness and half the channel width, $\epsilon = h/(w/2)$, while the dimensionless radius of curvature of the circular turns is $R = R_c/(w/2)$. For the study reported here we consider small values of the Reynolds numbers, which based on the length scale $w/2$, is $Re = (Uw/2)/\nu < 1$, where ν is the kinematic viscosity of the fluid, and include the limit of vanishingly small Reynolds numbers. Since we only consider $h/w = O(1)$, the common channel Reynolds number $(Uh)/\nu$ is also small in our simulations. This range of Reynolds numbers is typical of the experiments briefly described in §1 (figure 1) and, in general, of many microfluidic applications. For completeness, we also report some numerical result for $Re = O(1)$.

We obtain numerical solutions of the flow field in these geometries via finite-element simulations of the incompressible form of the Navier–Stokes equations performed using COMSOL software. The simulations employ pressure boundary conditions at the inlet and at the outlet and have been performed by choosing for each geometry the pressure drop that yields an average velocity equal to one. The numerical solutions have been validated via successive grid refinements (the meshes employed to obtain the results discussed in this work consist of at least 300 000 elements). We have verified the convergence of the solution with respect to the size of the computational domain and avoided geometric singularities by rounding sharp corners with fine fillets (when not specified, the radius of curvature of a 90° turn is $R = 0.05$). In particular, for a thin channel with $\epsilon = 0.1$, we typically used 40 elements across the small dimension. Also, for a few test cases, we compared our results with the solution provided by a second software package, TransAT, which uses a finite-volume method and an immersed boundary technique to solve the governing equations.

3. Flow structure near a three-dimensional corner

3.1. *The velocity distribution*

We first illustrate the basic features of low-Reynolds-number flows in three-dimensional confined corner geometries. To the best of our knowledge the detailed flow features we describe are little known, though numerical simulations, usually at moderate Reynolds numbers, of flow in three-dimensional geometries frequently showed complicated streamline patterns indicative of a regular secondary flow (Yi & Bau 2003). We begin with a case, where the cross-sectional aspect ratio is one half (i.e. $\epsilon = 1$) for a channel that has a sequence of either sharp or rounded turns. Typical flow solutions are given in figure 3, where the primary flow is moving from left to right. Sufficiently far from the corner the flow develops as a classical pressure-driven two-dimensional flow in a rectangular cross-section, $\boldsymbol{u} = u_x(y, z)\,\boldsymbol{e}_x$. However, in the neighbourhood of the corner or the turn, the flow becomes fully three-dimensional with well-defined features. In the following, we will present results in the form of contour plots, to convey three-dimensional information, and in the form of one-dimensional plots, to convey more quantitatively the trends and to describe the dependence of the secondary flow on the parameters of the problem.

In order to provide a complete description of the flow and to identify its characteristic features, we present the velocity field in cross-sectional planes. In particular, we interpret a non-vanishing u_z as the signature of a three-dimensional secondary flow. We will see that the trigger of this three-dimensional secondary flow is a change of the boundary curvature (e.g. Balsa 1998; Lauga *et al.* 2004). In figure 3(*a*), contour plots of the modulus of the velocity field $|\boldsymbol{u}|$ are shown in the middle plane of the channel ($z = 1/2$) and in two cross-sections for the case of a sequence of sharp turns. Here black contours indicate zero velocity and white contours indicate the maximum values of the velocity field. Streamlines are superimposed in order to help visualize the flow. In figure 3(*b*), for the same geometry, contour plots of the component of velocity orthogonal to the plane of the channel u_z are shown in the plane $z = 1/4$ and in several cross-sectional planes along the length of the channel. In this panel, grey contours indicate vanishing vertical velocity and white and black contours identify, respectively, upward and downward velocity. We observe that, in the neighbourhood of the corner, the flow is simply planar in the middle section of the channel, while, as soon as we leave this plane, the flow is three-dimensional and anti-symmetrical about the mid-plane (note the appearance of a white region with

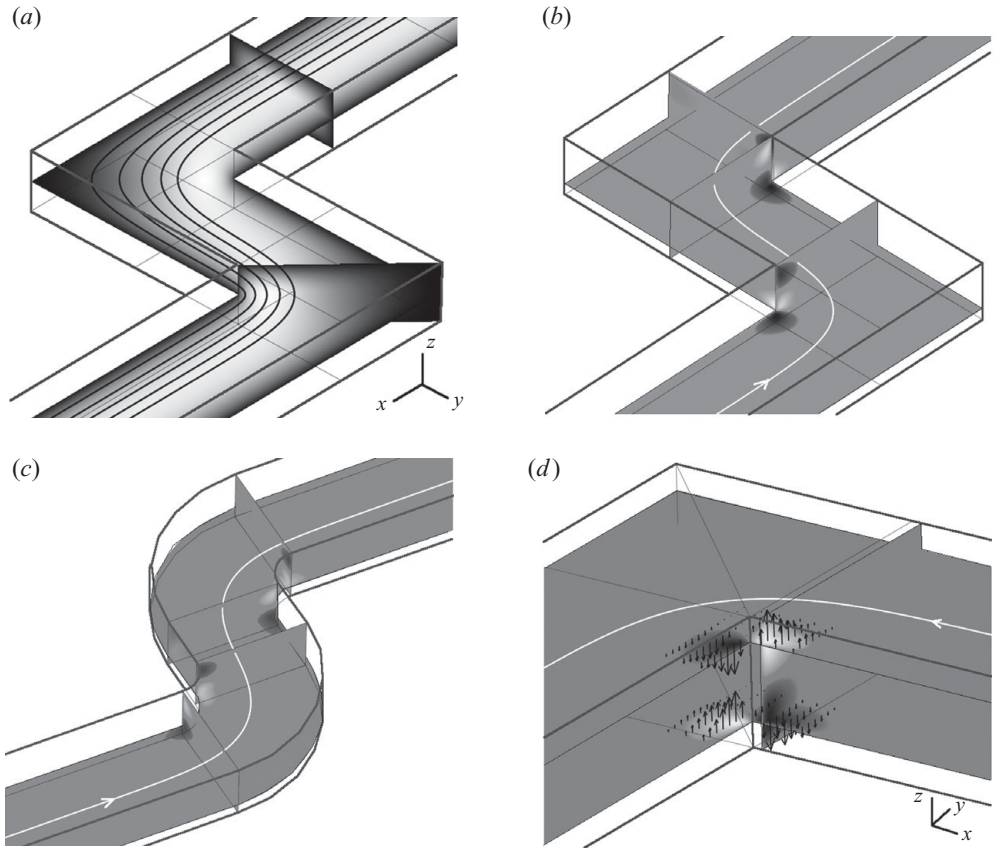

FIGURE 3. Pressure-driven flow (left to right) in channels characterized by a rectangular cross-section of dimensionless thickness $\epsilon = 1$ and (a, b, d) a sequence of sharp turns or (c) rounded turns with inner radius $R = \epsilon/2$. (a) Contour plots of the modulus of the velocity $|\boldsymbol{u}|$ in the plane $z = 1/2$ and in two cross-sectional planes, where dark colours indicate velocity near zero and white colour indicates the largest velocities. A few streamlines are drawn in order to help visualize the primary flow. (b, c) Contour plots of the velocity component u_z orthogonal to the middle plane of the channel in the plane $z = 1/4$ and in four planes at constant x or at constant y. Thicker lines identify channel boundaries, while thinner lines provide various planes and sections. White and black contours indicate, respectively, positive and negative values of u_z, and grey contours indicate vanishing values of u_z. (d) Detail of the flow field shown in (b), with contour plots of u_z in the planes $z = \{1/4, 3/4\}$ and in a cross-section located in the proximity of turn; arrows suggest the sign of the local velocity. In all of the simulations, the Reynolds number is $Re = 0.001$.

$u_z > 0$ on the top half of the channel upstream of the corner and on the bottom half of the channel downstream of the corner).

We next contrast the flow around sharp turns with that around rounded turns (figure 3c). Again we show contour plots of u_z in the plane $z = 1/4$ and in a number of cross-sectional planes. There are three important qualitative features to indicate: (i) in the region close to a change of the curvature of the side boundary the flow becomes three-dimensional, (ii) the structure of the flow appears qualitatively similar to the flow for the channel with sharp corners, and (iii) the secondary flow is in this case weaker than the secondary flow around sharp turns.

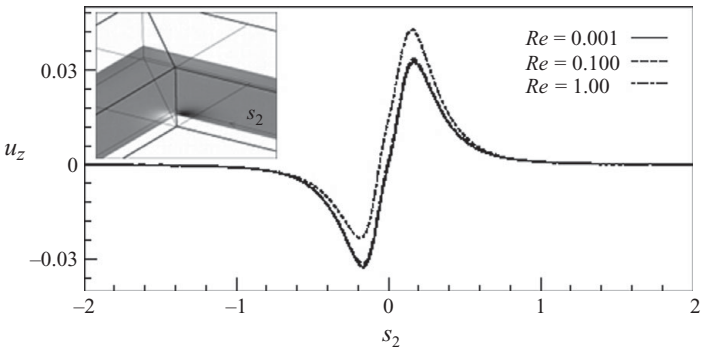

FIGURE 4. Pressure-driven flow in a channel characterized by a rectangular cross-section of dimensionless thickness $\epsilon = 1$ and a sharp 90° turn. $Re = 0.001, 0.1, 1$. Distribution of the component of the velocity orthogonal to the plane of the channel u_z along a line parallel to the inner side boundary of the channel (see inset), hence along the curvilinear coordinate s_2.

The fully three-dimensional flow field about a sharp corner is illustrated again in figure 3(*d*). A streamline is drawn to give the direction of the flow, from right to left. As the fluid approaches the turn, streamlines curve following the main channel direction and also bend slightly out of their initial plane. Fluid elements are deflected transversely to the main flow direction, in an anti-symmetrical fashion with respect to the middle plane of the channel (upward and downward arrows). Upon exiting the turn, fluid elements experience a deflection in the opposite direction, again in an anti-symmetrical fashion with respect to the symmetry plane of the corner. Hence, in two cross-sectional planes located right before and after the turn, we identify pairs of counter-rotating vortical structures, which we refer to as streamwise or open vortices, since the streamlines have a helical character. Note that the magnitude of the secondary flow is small (quantitative results are reported below), so it is difficult to capture in a plot the helical character of streamlines around a turn.

In order to determine those features of the observed behaviour that are inertial in nature, we evaluate the flow in the sharp corner geometry for increasing values of the Reynolds number. Figure 4 shows the distribution of the component of velocity orthogonal to the plane of the channel u_z along a line parallel to the inner side boundary of the channel (see inset of figure 4). We observe that the secondary flow is characterized by velocities that are a few per cent of the average velocity, which is consistent with the results reported by Lauga *et al.* (2004). For $Re \ll 1$ or even $Re < 1$ the velocity distribution is nearly independent of the Reynolds number. As the Reynolds number approaches unity, the flow becomes increasingly asymmetrical with respect to the position of the corner ($s_2 = 0$ in figure 4). Therefore, we conclude that the basic vortical flow phenomenon about the corner is inherently a viscous, i.e. zero Reynolds number, phenomenon.

The fact that an ordinary corner can give rise to a three-dimensional flow at zero Reynolds number is consistent with recent results in the literature. For example, Shankar (2000) and Gomilko *et al.* (2003) discuss the occurrence of corner eddies for a boundary-driven Stokes flow in a three-dimensional wedge, and Lauga *et al.* (2004) show that for a pressure-driven Stokes flow in a curved channel with rectangular cross-section the flow structure is inherently three-dimensional unless the channel has both constant curvature and constant cross-section. Finally, in a boundary-layer characterization of the Hele-Shaw geometries valid in the limit of small Reynolds

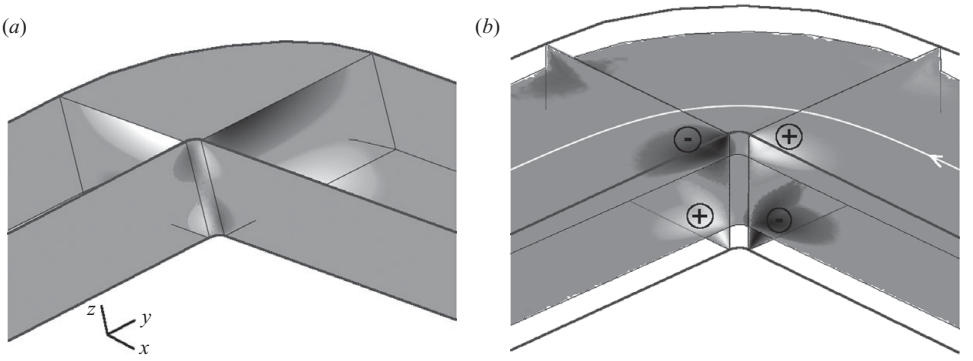

FIGURE 5. Pressure-driven flow in a channel of rectangular cross-section and dimensionless thickness $\epsilon = 1$, which has a 90° rounded turn of inner radius of curvature $R = 0.1$. $Re = 0.001$. (a) Contour plots of the component of the vorticity field along the curvilinear coordinate s_2, ω_{s_2}, evaluated at the sidewalls of the channel, at the bottom wall and over the two cross-sectional planes at $s_2 = \pm R\pi/4$ upstream and downstream of the corner. (b) Contour plots of the normalized helicity density $\boldsymbol{u} \cdot \omega/|\boldsymbol{u}||\omega|$ on the two planes $z = \{1/4, 3/4\}$ and on the two cross-sections at $s_2 = \pm R\pi/4$. For both plots white and back contours indicate, respectively, positive and negative values of the represented quantity and a streamline indicates the direction of the flow, from right to left.

numbers, Balsa (1998) interprets the secondary flow as due to viscous diffusion of the vorticity generated by a variation of the curvature of the boundary (see § 4).

3.2. *The vorticity distribution*

In order to provide a description of the flow structure in term of vorticity $\omega = \nabla \wedge \boldsymbol{u}$, we introduce the streamwise component ω_{s_2} along the curvilinear axis s_2 of the vorticity vector (see figure 2 for the direction s_2). In figure 5(a) we plot, for the case of a channel with a rounded turn of inner radius of curvature $R = 0.1$, the distribution of ω_{s_2} on the sidewalls of the channel, on the bottom wall, and on two cross-sections in the vicinity of the corner, for $s_2 = \pm R\pi/4$. Similar to figure 3(d), the flow is from right to left and white and black contours identify, respectively, positive and negative values of the streamwise vorticity ω_{s_2}. The basic results are similar to the trends identified for the u_z-variations in figure 3(d). As we move along the curvilinear coordinate s_2, at the inner wall ($s_1 = 0$), at any z coordinate different from 1/2, approaching the change in curvature there is a non-vanishing value of ω_{s_2}, which goes through a maximum, vanishes on the plane of symmetry of the corner, and appears again downstream with opposite sign. This vorticity distribution is directly related to the secondary flow, since we have $\omega_{s_2} = \partial u_{s_3}/\partial s_1$ at $s_1 = 0$. The distribution of vorticity ω_{s_2} on the two cross-sections $s_2 = \pm R\pi/4$ is primarily dominated by the contribution $\partial u_{s_1}/\partial s_3$, hence by the primary flow.

We find it convenient to characterize these three-dimensional flows in terms of the helicity, which is defined as $\boldsymbol{u} \cdot \omega$. This quantity is non-zero when the vorticity is aligned with the local velocity vector and for these channel flow evidently indicates the onset of a three-dimensional helical flow structure. We chose to work with the normalized helicity density $\boldsymbol{u} \cdot \omega/|\boldsymbol{u}||\omega|$. Contour plots of the normalized helicity density in the two planes at $z = \{1/4, 3/4\}$ and in the two cross-sections $s_2 = \pm R\pi/4$ are shown in figure 5(b). Again white and black contours identify, respectively, positive and negative values of the helicity, which directly provide the sign of the spiralling motion. The results suggest that the secondary flow is characterized by a single vortex (either

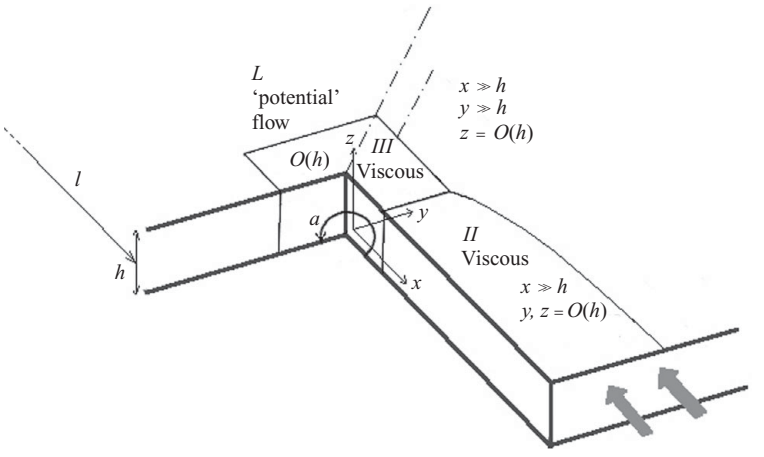

FIGURE 6. Schematic of the geometry discussed in § 4: a semi-infinite domain is bounded by two plane walls and two sidewalls, which span the gap between the two plane walls and intersect at an angle α. Grey thick lines draw the boundary of the geometry and arrows suggest the direction of the undisturbed flow. All the geometric quantities are dimensional in this figure. We introduce a Cartesian reference frame (x, y, z) and identify three distinct regions in which different assumptions concerning the fluid flow hold.

positive helicity or negative helicity as indicated in the figure) per corner formed by the sidewall with the top or bottom wall. Given the symmetry of the problem, we can conclude that in a pressure-driven flow between two plane walls and around two consecutive sidewalls that form a 270° corner, as measured through the fluid, two pairs of counter-rotating vortices, anti-symmetrical with respect to the symmetry plane of the corner and of the middle plane of the channel, are formed.

In § 5, we provide additional numerical results and discuss how the secondary flow depends on the significant geometric parameters, i.e. the aspect ratio of the channel cross-section, the radius of curvature of the corner, and the variation of curvature of the side boundary. In addition, we compare numerical results with predictions from an asymptotic description, which is introduced in the next section.

4. A boundary layer description of the low-Reynolds-number flow around a three-dimensional corner

With the aim of providing a more quantitative insight into the secondary flow, we outline a matched asymptotic expansion solution for the three-dimensional corner flow, which finds inspiration and benefits from the general approach developed by Balsa (1998) for flow around an object of cylindrical shape in a Hele-Shaw configuration (see also Thompson 1968). The basic features of the corner flow are sketched in figure 6. We consider the channel geometry (figure 2) in the limit of a wide channel, $\epsilon \ll 1$, i.e. we consider the flow field in the region bounded by two plane parallel walls and two sidewalls, which span the gap between the two parallel walls and intersect at an angle α.

It is useful to introduce a short-hand notation for discussing the three-dimensional flow. For some part of the discussion we adopt a Cartesian (x, y, z) description, while for another a cylindrical coordinate description (r, θ, z) is useful. When we focus on variations across the short dimension (z-axis) or variations in the plane parallel to the mean flow direction (when viewed from above) we use $\boldsymbol{x} = \boldsymbol{x}_{\parallel} + z\,\boldsymbol{e}_z$. Alternatively,

when we focus on the three-dimensional variations that occur in a cross-section as the corner is approached from the upstream, following streamlines that run nearly parallel along the boundary (x-axis), we write $\boldsymbol{x} = \boldsymbol{x}_\perp + x\,\boldsymbol{e}_x$. Correspondingly, gradients are denoted $\nabla = \nabla_\parallel + \boldsymbol{e}_z\,\partial/\partial z$ or $\nabla = \nabla_\perp + \boldsymbol{e}_x\,\partial/\partial x$, and the velocity vector is denoted $\boldsymbol{u} = \boldsymbol{u}_\parallel + u_z\boldsymbol{e}_z$ or $\boldsymbol{u} = \boldsymbol{u}_\perp + u_x\boldsymbol{e}_x$. Note that in the following we utilize dimensionless variables in the asymptotic solution, but for simplicity we retain the same notation.

4.1. *The outer 'potential' flow*

With reference to figure 6, we identify an 'outer' region *I*, labelled 'potential' flow in the figure, where the characteristic length scale in the streamwise direction x, as well as in the cross-stream direction y, is denoted $\ell = O(w)$, and the characteristic length scale along the orthogonal z-direction is h. In this region, we find the traditional 'potential' flow description of the Hele-Shaw geometry. Let the velocities and pressure be normalized, respectively, by U and $\mu U\ell/h^2$ and pose an expansion in the small parameter $\delta = h/\ell \ll 1$. Now, using dimensionless variables, we write

$$\boldsymbol{u}_\parallel = \boldsymbol{u}_\parallel^{(0)} + \delta\boldsymbol{u}_\parallel^{(1)} + \cdots, \quad u_z = \delta^\beta\left(u_z^{(0)} + \delta u_z^{(1)} + \cdots\right), \quad p = p^{(0)} + \delta p^{(1)} + \cdots, \tag{4.1}$$

where all the variables depend at most on the outer coordinates (x, y, z) and we want $\beta > 1$. Note that, as compared with the notation introduced earlier, $\delta = O(\epsilon)$ but, because of the focus here on an isolated corner, to avoid confusion we have introduced the small parameter δ. The lowest order outer governing equations are

$$\frac{\partial^2\boldsymbol{u}_\parallel^{(0)}}{\partial z^2} = \nabla_\parallel p^{(0)}, \tag{4.2a}$$

$$\frac{\partial p^{(0)}}{\partial z} = 0, \tag{4.2b}$$

$$\nabla_\parallel \cdot \boldsymbol{u}_\parallel^{(0)} = 0. \tag{4.2c}$$

which are four equations for the four unknowns $p^{(0)}$, $\boldsymbol{u}_\parallel^{(0)}$, $u_z^{(0)}$, with $u_z^{(0)} = 0$. Hence, $\nabla_\parallel^2 p^{(0)} = 0$. This problem is best studied by using cylindrical coordinates, in which case, satisfying $\boldsymbol{u}_\parallel^{(0)} = \boldsymbol{0}$ at $z = 0, 1$, yields

$$\boldsymbol{u}_\parallel^{(0)}(r, \theta, z) = -\frac{(z - z^2)}{2}\nabla_\parallel p^{(0)}, \tag{4.3}$$

and

$$p^{(0)} = r^\lambda f(\theta), \quad \text{with} \quad f(\theta) = A\,\cos(\lambda\theta) + B\,\sin(\lambda\theta), \tag{4.4}$$

which is a well-known result when considering potential flow around a corner. We can only apply a boundary condition on the normal component of velocity at the walls $\theta = \{0, \alpha\}$, which corresponds to $\mathbf{n}\cdot\nabla_\parallel p = 0$, or $\partial p/\partial\theta = 0$ and yields the eigenvalues λ. Therefore, we find $B = 0$ and the smallest eigenvalue is $\lambda = \pi/\alpha$. This result does not satisfy the no-slip boundary condition at the walls, $\theta = \{0, \alpha\}$, where $u_r^{(0)} = u_x^{(0)} \neq 0$. This slip flow drives motion in the viscous boundary layer, adjacent to the sidewall, which characterizes the region '*II* viscous' in figure 6. In this boundary region

$$\frac{\partial p^{(0)}}{\partial x} \propto \lambda x^{\lambda-1}, \tag{4.5a}$$

$$u_x^{(0)} \propto -\frac{(z - z^2)}{2}\lambda x^{\lambda-1}. \tag{4.5b}$$

4.2. *A 'geometric' boundary layer*

Next, we identify an 'inner' region, denoted as '*II* viscous' in figure 6, such that h is the significant scale both along z and y axes. Given the focus on the symmetry of the geometry, we need to consider only the region $0 \leqslant \theta \leqslant \alpha/2$. Hence, we define the dimensionless inner coordinates $(\hat{x}, \hat{y}, \hat{z})$, where the different scaling than in the outer region leads to $\hat{y} = y/\delta = O(1)$, with y the dimensionless coordinate for the outer region. For the sake of completeness, we note that we expect the existence of a further inner region, denoted as '*III* viscous' in figure 6, where h is the appropriate scale for all three directions x, y, z. We have not succeeded in analysing this innermost portion of the flow domain, since it appears to require consideration of the full Stokes equation.

For region '*II* viscous', using the defined inner variables, we represent the expansion of the velocity and pressure fields as (for further details, see the Appendix)

$$\hat{u}_x = \hat{u}_x^{(0)} + \delta\hat{u}_x^{(1)} + \cdots, \quad \hat{\boldsymbol{u}}_\perp = \delta\left(\hat{\boldsymbol{u}}_\perp^{(0)} + \delta\hat{\boldsymbol{u}}_\perp^{(1)} + \cdots\right), \quad \hat{p} = \hat{p}^{(0)} + \delta\hat{p}^{(1)} + \delta^2\hat{p}^{(2)} + \cdots. \tag{4.6}$$

After substituting (4.6) into the governing momentum and continuity equations and collecting like powers of δ, we identify the leading-order inner problem

$$\nabla_\perp^2 \hat{u}_x^{(0)} = \frac{\partial \hat{p}^{(0)}}{\partial \hat{x}}, \tag{4.7a}$$

$$\nabla_\perp^2 \hat{\boldsymbol{u}}_\perp^{(0)} = \nabla_\perp \hat{p}^{(2)}, \tag{4.7b}$$

$$\frac{\partial \hat{u}_x^{(0)}}{\partial \hat{x}} + \nabla_\perp \cdot \hat{\boldsymbol{u}}_\perp^{(0)} = 0, \tag{4.7c}$$

with $\nabla_\perp^2 = (\partial^2/\partial\hat{y}^2 + \partial^2/\partial\hat{z}^2)$. This problem statement is completed by imposing no-slip boundary conditions at the walls and by requiring for $\hat{y} \to \infty$ the streamwise velocity $\hat{u}_x^{(0)}$ match the outer velocity component $u_x^{(0)}$. Also, following Balsa (1998), the inner asymptote of the outer pressure distribution, including an additional term $\delta p^{(1)}$, provides the behaviour of the pressure in the inner region as $\hat{y} \to \infty$, which we denote p^I. Therefore, in inner variables the pressure distribution as $\hat{y} \to \infty$ is

$$\hat{p}_\infty = \lim_{y\to 0} p(x, y) = p^{I(0)}(\hat{x}) + \delta\, p^{I(1)}(\hat{x}) + \delta^2\, p^{I(2)}(\hat{x}, \hat{y}) + \cdots. \tag{4.8}$$

Since from momentum equation $\partial\hat{p}^{(0)}/\partial\hat{y} = O(\delta^2)$, then we have for the component of velocity along $\hat{x}$

$$\nabla_\perp^2 \hat{u}_x^{(0)} = \frac{\partial \hat{p}^{(0)}}{\partial \hat{x}} = \frac{\mathrm{d}\, p^{I(0)}}{\mathrm{d}\hat{x}}, \quad \hat{u}_x^{(0)}(\hat{x}, \hat{y} \to \infty, \hat{z}) = -\frac{(z - z^2)}{2}\frac{\mathrm{d}\, p^{I(0)}}{\mathrm{d}\hat{x}}, \tag{4.9}$$

along with homogeneous boundary conditions at the walls, $\hat{u}_x^{(0)}(\hat{x}, \hat{y} = 0, \hat{z}) = 0$, $\hat{u}_x^{(0)}(\hat{x}, \hat{y}, \hat{z} = \pm 1) = 0$.

For the solution of (4.7) for the components of velocity $\hat{\boldsymbol{u}}_\perp^{(0)}$, we follow the approach of Balsa (1998) and define

$$\hat{p}^{(2)} = \hat{p}_\infty^{(2)} + \hat{p}^*, \tag{4.10a}$$

$$\hat{\boldsymbol{u}}_\perp^{(0)} = \hat{\boldsymbol{u}}_{\perp\infty}^{(0)} + \hat{\boldsymbol{u}}_\perp^*, \tag{4.10b}$$

where the components $(\hat{})_\infty^{()}$ satisfy the matching conditions for $\hat{y} \to \infty$ and can be easily determined from the characteristics of the outer 'potential' flow, and the components $(\hat{})^* \to 0$ as $\hat{y} \to \infty$. By additionally requiring that the total mass source in a cross-section is zero, we finally write for the components of velocity $\hat{\boldsymbol{u}}_\perp^* = (\hat{u}_y^*, \hat{u}_z^*)$,

which identifies the 'secondary' flow produced by the boundary, the following set of equations

$$\nabla_\perp^2 \hat{\boldsymbol{u}}_\perp^* = \nabla_\perp \hat{p}^*, \tag{4.11a}$$

$$\nabla_\perp \cdot \hat{\boldsymbol{u}}_\perp^* = -\frac{\mathrm{d}^2 p^{I(0)}}{\mathrm{d}\hat{x}^2} \sum_{n=1,3,5..}^{\infty} A_n \sin n\pi\hat{z}\, \mathrm{e}^{-n\pi\hat{y}}, \tag{4.11b}$$

where the $\{A_n\}$ are defined in (A 10). We thus obtain a mathematical problem that closely resembles the problem identified and solved in Balsa (1998) for the 'secondary' flow. For the sake of brevity we note that, given the parametric dependence of the problem on the streamwise coordinate $\hat{x}$, it is convenient to look for a solution in the form

$$\hat{u}_x^{(0)}(\hat{x}, \hat{y}, \hat{z}) = \frac{\mathrm{d}\, p^{I(0)}}{\mathrm{d}\,\hat{x}} f_{\hat{x}}(\hat{y}, \hat{z}), \tag{4.12a}$$

$$\hat{\boldsymbol{u}}_\perp^*(\hat{x}, \hat{y}, \hat{z}) = \frac{\mathrm{d}^2 p^{I(0)}}{\mathrm{d}\hat{x}^2} \boldsymbol{f}_\perp(\hat{y}, \hat{z}). \tag{4.12b}$$

More details about the various steps that appear in the problem description given by (4.9), (4.11) and (4.12), and about the structure of the functions $f_{\hat{x}}$ and $\boldsymbol{f}_\perp$ are provided in the Appendix.

We anticipate that the solution for the 'geometric' boundary layer described here captures the main quantitative features of the secondary flow in the region denoted with '*II* viscous', i.e. approaching the corner and leaving the corner, with the exception of the innermost region '*III* viscous', where none of the spatial derivatives can be considered negligible. Also, from (4.8) and (4.12), and from the distribution of pressure in the potential flow, $p^{(0)} = Ar^\lambda \cos(\lambda\theta)$, it follows that the secondary flow is antisymmetric with respect to the plane of symmetry of the geometry, $\theta = \alpha/2$, a fact that has already been noted while commenting on the numerical results.

While describing the numerical results, we have characterized the secondary flow mainly in terms of the component of velocity orthogonal to the plane of the geometry u_z, and consequently, we are interested in comparing the numerical results with the analytical results developed in this section for $\hat{u}_z^*$. From (4.8) and (4.12*b*) and from the expression of the outer pressure (4.5*a*), we observe that the inner zero-order solution predicts a dependency of $\hat{u}_z^*$ on the streamwise coordinate x of the form $\hat{u}_z^* \propto x^{\lambda-2}$. A similar behaviour should be expected for the streamwise vorticity at the wall, denoted as ω_{s_2} in § 3, which for the geometry under consideration corresponds to the component $\hat{\omega}_x \boldsymbol{e}_x = \nabla_\perp \wedge \hat{\boldsymbol{u}}_\perp$. From a more detailed study of the solution for $\hat{u}_z^*$, we also verify that the $\hat{u}_z^*$ distribution is antisymmetric (or odd) with respect to middle horizontal plane of the channel $z = 1/2$. In addition, we find that $\hat{u}_z^*$ should decay approximately exponentially with the distance from the sidewall y according to $\hat{u}_z^* \approx \exp(-2\pi\, y/\delta)$ for $y \gg \delta$. In § 5, we compare these asymptotic results with the results from the numerical simulations.

5. Analysis of the secondary flow

5.1. *Dependence of the flow on the aspect ratio of the channel cross-section*

For a channel geometry characterized by a nearly sharp 90° turn, we systematically vary the thickness ϵ for a fixed channel width, thus varying the aspect ratio of the channel cross-section. Figure 7 shows perspective views of the velocity field for three different geometries, characterized by $\epsilon = \{0.5, 2, 4\}$, respectively. In order to

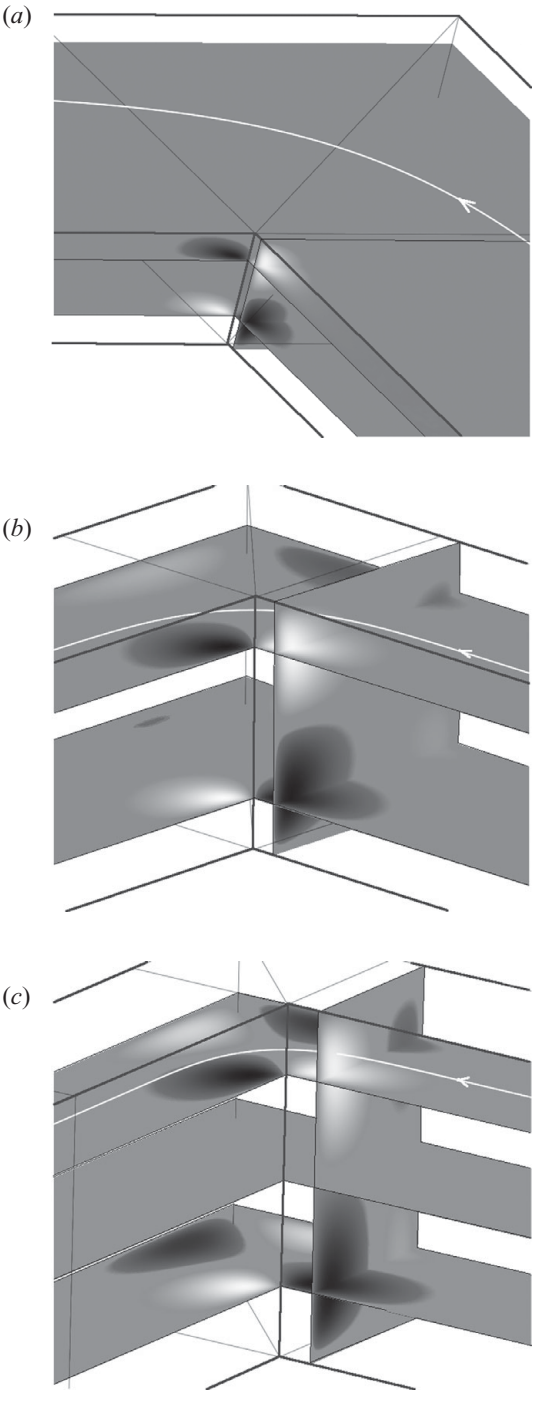

FIGURE 7. Pressure-driven flow in channels with rectangular cross-section of constant width and thickness $\epsilon = \{0.5, 2, 4\}$ (from *a*–*c*), with the inner radius of curvature of the turn $R = 0.05$. $Re = 0.001$. For each geometry, contour plots of the component of velocity orthogonal to the plane of the channel u_z on two or three planes at constant z and in a cross-sectional plane located right before the turn are shown. White, black and grey contours represent, respectively, positive, negative and vanishing values of u_z. The flow is from right to left.

provide a complete description of the spatial distribution of the secondary flow, each image shows the contour plot of the component of velocity u_z orthogonal to the plane of the channel in two planes at $z = \{1/4, 3/4\}$ and in a cross-sectional plane located just upstream the corner. For all of the geometries the secondary flow, where present, develops over the whole thickness of the channel and its extension, in each direction upstream and downstream, is approximately half the channel thickness.

With focus on the vortical structures, we note that the secondary flow induced at the outer corner, even if less intense than that around the inner corner, is nevertheless always present; such secondary motions are more evident for larger thicknesses of the channel. For $\epsilon = 4$ (figure 7*c*), an identifiable secondary flow in the streamwise direction is clearly seen at both the inner and outer corners and occupies the entire cross-section of the channel.

In order to gain a more quantitative description of the secondary flow and its dependence on the cross-sectional aspect ratio ϵ, we consider the distribution of the streamwise vorticity ω_{s_2} along the inner sidewall of the channel for the various geometries. Figure 8(*a*) shows the modulus of ω_{s_2}, averaged over the channel thickness, plotted versus the curvilinear coordinate s_2, for several values of the parameter ϵ. These vorticity distributions, scaled with the channel thickness, are plotted versus s_2/ϵ on a linear scale in figure 8(*b*), and as a log–log graph in figure 8(*c*). With the rescaling introduced in figure 8(*b*), the vorticity profiles for the various geometries nearly collapse, though there are small differences in the slope of the various curves, which increases for increasing values of ϵ. A reason for this variation can be found in the fact that the radius of curvature of the turn for various geometries is constant (here equal to 0.05), so that the ratio R/ϵ, hence the 'sharpness' of the turn, varies. Moreover, in figure 8(*c*) the vorticity at the sidewall along s_2/ϵ is compared, in a log–log plot, with the behaviour predicted by our theoretical analysis, i.e. a power-law decay with exponent $(\lambda - 2) = -4/3$ (see (4.12*b*), (A 5*a*) and (4.5*a*)), since $\lambda = 2/3$ for flow outside the 90° corner (a 270° corner when measured through the fluid domain). The agreement between the numerical curves and the asymptotic prediction is satisfactory within the region '*II* viscous', where our asymptotic approach is valid, i.e. for s_2/ϵ large enough.

Rather than considering a surface value of the vorticity, we provide a measure of the variation with the distance from the corner of the values of the velocity component u_z. In figure 9 we plot u_z along three rectilinear lines, parallel to each of the coordinate axes (x, y, z) and passing through the location where u_z is a minimum (see inset in figure 9). More precisely, for all the geometries we plot u_z versus x/ϵ at the same distances from the bottom and sidewalls scaled with the channel thickness, respectively $z/\epsilon = \bar{z}$ and $y/\epsilon = \bar{y}$ (figure 9*a*). We then identify for each geometry the coordinate $\bar{x}_\epsilon$ where u_z reaches a minimum and on that cross-section we plot u_z versus the transverse coordinate z/ϵ at $y/\epsilon = \bar{y}$ and u_z versus the cross-stream coordinate y/ϵ at $z/\epsilon = \bar{z}$ (figure 9*b*,*c*). The velocity profiles obtained in this way along the three directions superimpose, to a good approximation, with the exception of the case with $\epsilon = 4$. We note in figure 9(*a*) that, while all the u_z curves decay to zero velocity far from the corner at about the same rate, the position of the minimum of velocity along x/ϵ changes (the quantity we denoted $\bar{x}_\epsilon$). Again, this variation is likely due to the fact that the geometries have different ratios R/ϵ; for increasing ϵ, R/ϵ decreases, the turn becomes 'sharper' and the point of maximum velocity approaches the corner. Moreover, as already indicated, for the case of the channel with thickness $\epsilon = 4$, the secondary flow at the inner turn is modified by the vicinity of the outer sidewall and velocity profiles are significantly different from those for smaller values of ϵ.

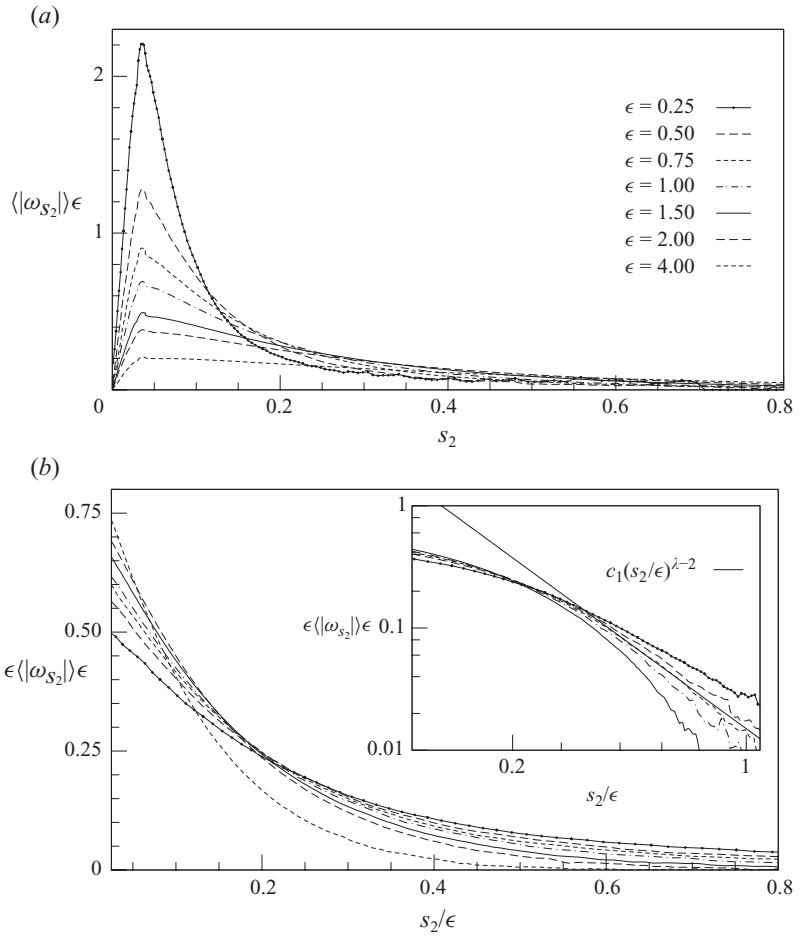

FIGURE 8. Pressure-driven flow in channels with rectangular cross-section of constant width and thickness $\epsilon = 0.25$–4. The inner radius of curvature of the turn is $R = 0.05$. $Re = 0.001$. (*a*) Modulus of the component of the vorticity along s_2 evaluated at the inner sidewall of the channel, averaged over the channel thickness, versus the curvilinear coordinate s_2. (*b*) The same result as in (*a*), but scaled with the channel thickness is plotted versus the coordinate s_2, also scaled with the channel thickness ϵ. The average streamwise vorticity at the inner sidewall, scaled with ϵ, is plotted on a log–log scale versus s_2/ϵ. The results are compared with the theoretical prediction, $\omega_{s_2} \propto c_1(s_2/\epsilon)^{\lambda-2}$, with $\lambda = 2/3$ for the case of a 270° corner in the fluid domain.

Also, we compare the behaviour of u_z predicted by the geometric boundary-layer approach introduced in §4 with the distribution of the component of velocity u_z as obtained from the numerical simulations (figure 9). In particular, the velocity profiles along the streamwise direction x compares well with the predicted power-law profile $x^{\lambda-2}$ for values of the channel thickness $\epsilon \leqslant 1$, as shown by the three analytical curves for $\epsilon = \{0.25, 0.5, 1\}$ in (figure 9*a*). Also, along the cross-stream direction y the decay of the u_z velocity distribution computed for different channel geometries approximately follows the exponential decay $\exp(-2\pi y/\epsilon)$ predicted by the analytical solution.

Based on the presented results we conclude that over a range of the dimensionless thickness ($0 < \epsilon \leqslant 2$), the most significant dimension in the description of the secondary flow is the channel thickness. When the channel thickness is larger than

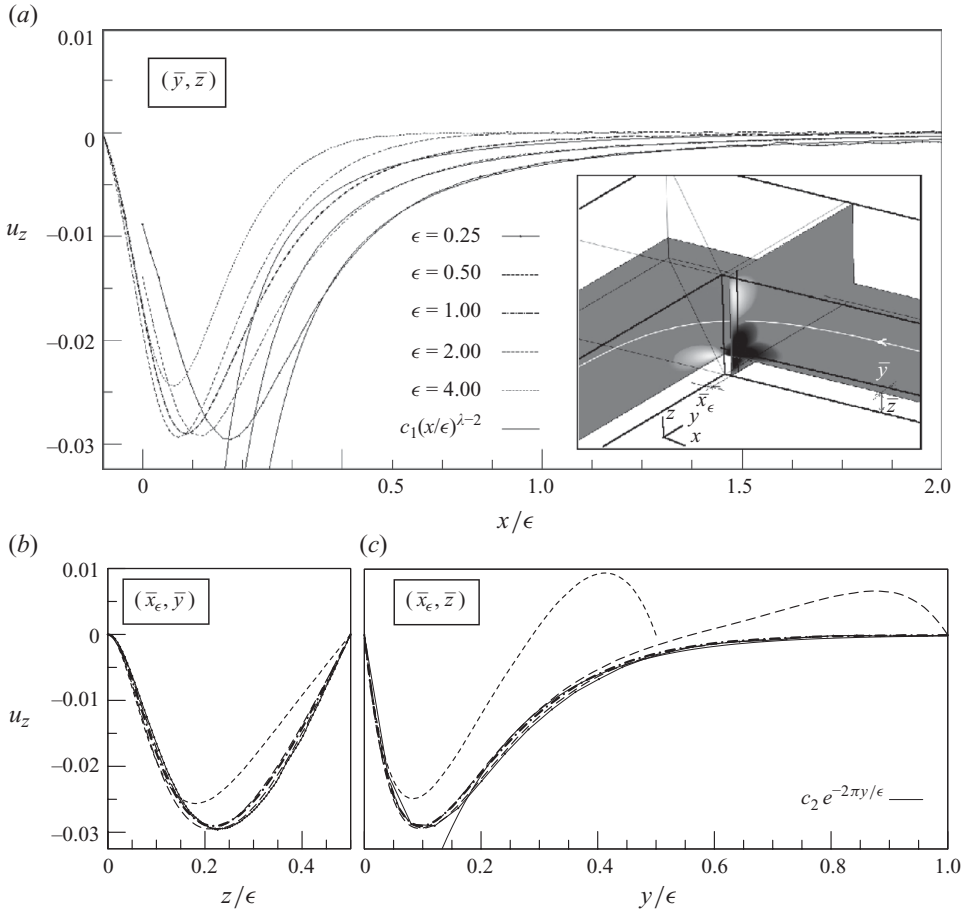

FIGURE 9. Pressure-driven flow in channels with rectangular cross-section of constant width and thickness $\epsilon = 0.5$–4, and inner radius of curvature of the turn $R = 0.05$. $Re = 0.001$. (*a*) Component of velocity orthogonal to the plane of the channel u_z versus x/ϵ at distances from the bottom and sidewalls equal to $z/\epsilon = \bar{z}$ and $y/\epsilon = \bar{y}$, respectively, with $\bar{z}$ and $\bar{y}$ picked such that u_z its has minimum value. For the velocity distributions corresponding to $\epsilon = 0.25, 0.5$ and 1, we have added a comparison with the power-law response $c_1 x^{\lambda-2}$, with $\lambda = 2/3$ for this geometry, as suggested by asymptotic analysis (see §4.1). For each geometry, the coordinate $\bar{x}_\epsilon$ where u_z has a minimum, is identified. (*b*) Component of velocity u_z versus z/ϵ along a line at $x = \bar{x}_\epsilon$, $y/\epsilon = \bar{y}$. (*c*) Component of velocity u_z versus y/ϵ along a line at $x = \bar{x}_\epsilon$, $z/\epsilon = \bar{z}$. The plot also compares the numerical results with the behaviour of the component u_z along the cross-stream coordinate y predicted by the asymptotic approach, i.e. an exponential decay with ratio 2π. Again the agreement is satisfactory for $\epsilon = 0.25$–1 and outside of the most inner region.

the width ($\epsilon > 2$), then the latter also becomes relevant in the description of the secondary flow. In the remaining part of our discussion we will consider geometries characterized by dimensionless thickness $\epsilon = 1$, with the understanding that results will be valid over the identified range of channel thickness ($\epsilon \leqslant 2$).

5.2. *Dependence of the flow on the radius of curvature for a rounded turn*

Next we consider more details of the geometry in which a 90° turn (270° turn in the fluid domain) is formed by connecting two straight sections of a channel with a portion of an annular channel (see figure 2*b*), which gives a corner of constant (inner)

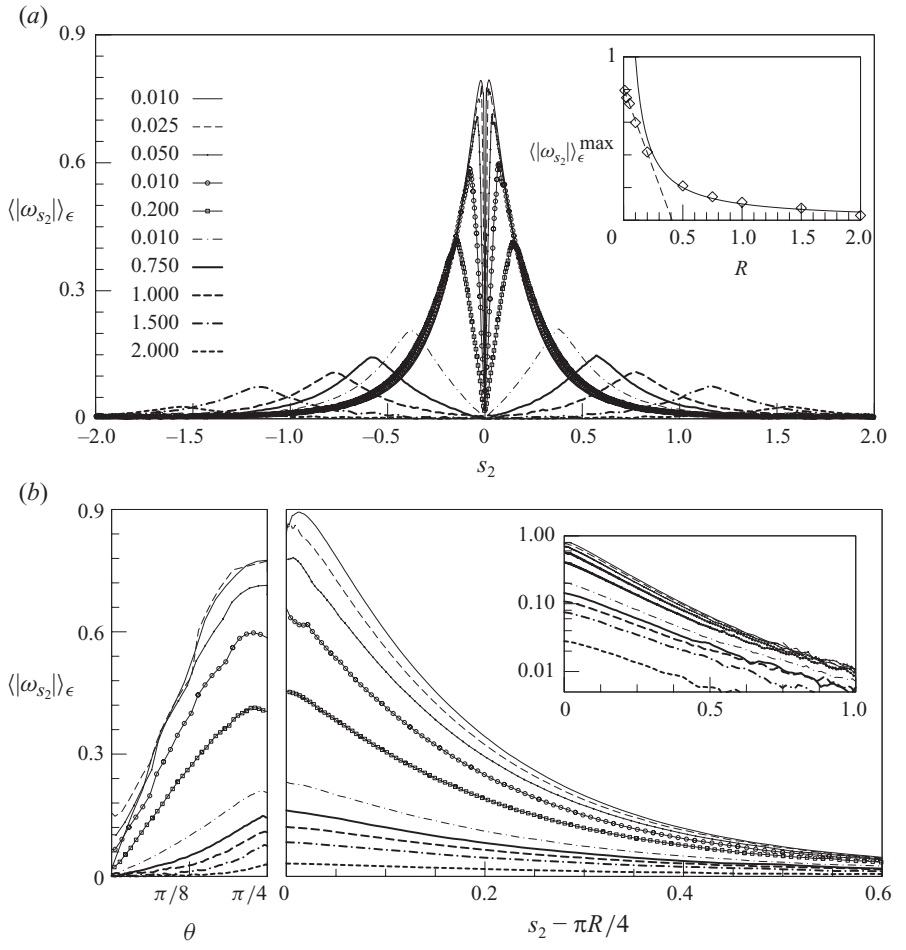

FIGURE 10. Pressure-driven flow in channels with rectangular cross-section of aspect ratio $\epsilon = 1$, inner radius of curvature of the turn $R = 0.025$–2. $Re = 0.001$. (*a*) Absolute value of the component of the vorticity along s_2 at the inner sidewall of the channel, averaged over the channel thickness and denoted $\langle|\omega_{s_2}|\rangle_\epsilon$, versus the curvilinear coordinate s_2, for different values of the radius of curvature R. The maximum of the average of $\omega_{s_2}|_{s_1=0}$ over the channel thickness is plotted versus the radius of curvature of the turn R; the numerical results over the interval $R = 0$–0.2 are fitted by the line $c_2 - c_1 R$ (dashed curve), while the vorticity maxima over the interval $R = 0.5$–2 are fitted by the curve $0.1/R$ (continuous curve). (*b*) The same results as in (*a*) are plotted versus the angular position along the turn θ (left), where $\theta = 0$ at the symmetry plane of the corner, and versus the distance from the point where the straight portion of the channel is connected with the curved section, $s_2 - \pi R/4$. The vorticity distributions along $s_2 - \pi R/4$ are plotted in a log-linear graph.

radius of curvature R. The qualitative features of the flow field for this particular geometry are shown in figures 3(*c*) and 5 and have already been described. Here we systematically increase the radius of curvature of the turn R and study the influence on the secondary flow.

Again we quantitatively describe the secondary flow by mean of the distribution of the streamwise vorticity along the sidewall of the channel. Figure 10(*a*) shows, for different values of the radius of curvature of the channel turn R, the distribution of the modulus of ω_{s_2} averaged over the thickness, $\langle|\omega_{s_2}|\rangle_\epsilon$, along the curvilinear

coordinate s_2. This vorticity distribution is characterized by two peaks, symmetrical with respect to the symmetry plane of the turn ($s_2 = 0$), in agreement with the three-dimensional vorticity distribution shown in figure 5(a). The same distribution of vorticity is also shown in figure 10(b) as a function of the angular position along the turns ($0 < \theta < \pi/4$, with $\theta = 0$ at $s_2 = 0$), and of the distance from the point at which the straight portion of the channel is connected to the turn, $s_2 - \pi R/4$. Not surprisingly, the maximum of vorticity always occurs for $\theta = \pi/4$, i.e. at the discontinuity in the curvature of the sidewall.

It is clear that the modulus of the streamwise vorticity decreases monotonically when the radius of the turn R is increased. In figure 10(a), we plot the maximum values of the average streamwise vorticity at the wall for the various geometries considered. The dashed and continuous curves fit the vorticity variation as function of radius of curvature R over two different ranges of R. In particular, we find that, for sufficiently small R ($R \leqslant 0.2$), the maximum of the wall vorticity approaches linearly the value computed for the most "sharp" corner geometry. For larger values of the radius of curvature, $R \simeq O(\epsilon)$, the maximum of the wall secondary vorticity decays approximately as $1/R$.

5.3. *Dependence of the flow on the curvature of the sidewall of the channel*

As mentioned in § 1, Balsa (1998) studied the flow past a long slender object spanning two parallel plates and showed that, in the limit of slow boundary perturbations and small Reynolds numbers, the strength of the streamwise vorticity associated with the secondary flow is determined by the rate of change of the curvature of the boundary. More precisely, for smooth geometries the second derivative with respect to the streamwise direction of the pressure at the sidewall, which determines the sign and the strength of the secondary streamwise vorticity (e.g. see (4.12b)), is proportional to the third derivative of the boundary shape. This result is consistent with other studies showing that, in bounded flows, where the geometry has a constant curvature (e.g. the annular space formed by two concentric cylinders) the flow is unidirectional, i.e. there is no secondary flow (Lauga *et al.* 2004).

Next, we evaluate the three-dimensional pressure-driven flow in a channel in which two straight sections are connected by a section characterized by wavy sidewalls. One of the sidewalls describes a sine wave of small amplitude, while the opposite wall is shaped in order for the channel cross-section to remain constant. We find that along the sidewalls the intensity of the secondary flow is proportional to the rate of change of the curvature of the boundary, as predicted by the asymptotic analysis, and additional secondary vorticity is produced at discontinuities. To illustrate this result and to provide a general idea of the structure of the secondary flow we show in figure 11(a) contour plots of the component of the velocity orthogonal to the plane of the channel u_z at the planes $z = \{1/4, 3/4\}$ and in a cross-section. In figure 11(b), we compare the behaviour of the streamwise vorticity ω_{s_2} at the sinusoidal sidewall along the coordinate x with that of the curvature of the sidewall $k(x)$ and of its derivative $k_{,x}$. Clearly, the vorticity changes sign when the derivative of the curvature changes sign, and if we evaluate the ratio between the two quantities, we find that it is approximately constant along the streamwise coordinate x (figure 11b, middle panel). This result is only not true in the vicinity of the points where the wavy section of the channel is connected to the straight sections, such that we have a jump in the local value of the curvature and its derivative is not defined.

For the case of sinusoidal sidewalls, for the chosen parameters, the assumption of slow boundary perturbation holds, and so the agreement between the computed

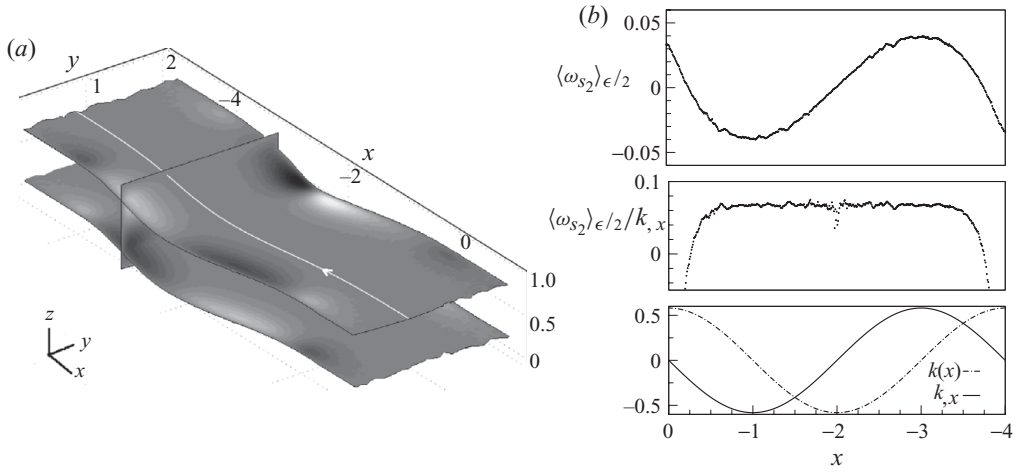

FIGURE 11. Pressure-driven flow in a channel with rectangular cross-section of dimensionless thickness $\epsilon = 1$ and characterized by a wavy portion, where one of the sidewalls (on the left in figure a) describes a whole sine wave of small amplitude, $f(x) = 1.15–0.15\cos\pi x/2$. $Re = 0.001$. (*a*) Contour plots of the component of velocity orthogonal to the plane of the channel u_z on two planes at constant z and in a cross-sectional plane are shown. White, black and grey contours represent, respectively, positive, negative and vanishing values of u_z. The flow is from right to left, as suggested by the streamline. (*b*) From top to bottom: component of the vorticity along s_2 at the left sidewall of the channel, averaged over half the channel thickness, versus the streamwise coordinate x; ratio between the defined quantity $\langle\omega_{s_2}\rangle_{\epsilon/2}$ and the derivative of the sidewall curvature $k_{,x}$; for the left sidewall, curvature $k(x) = f_{,xx}$ and derivative of curvature $k_{,x}$ versus the streamwise coordinate x.

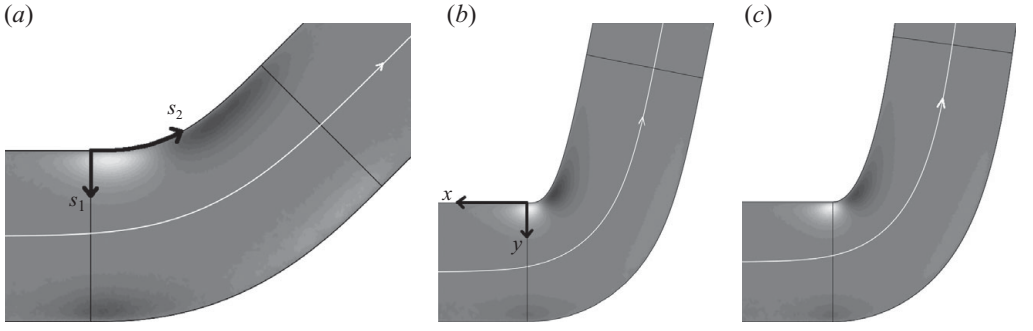

FIGURE 12. Pressure-driven flow in three similar channels with rectangular cross-section of aspect ratio $h/w = 1/2$ and characterized by a curved section, where the left sidewall is described by the shape function, $f(x) = \{-x^3(4+x)/16, 5-x^3(2+x)/2, \cosh 2x\}$. $Re = 0.001$. Contour plots of the component of velocity orthogonal to the plane of the channel u_z on a plane at constant z, located, where a strong secondary flow is present, are shown for every geometry. White, black and grey contours represent, respectively, positive, negative and vanishing values of u_z. The flow is from left to right, as suggested by the streamlines.

secondary flow and Balsa's (1998) prediction is not surprising. Next we discuss to what extent Balsa's theory can provide a criteria to understand secondary vorticity induced by more abrupt changes in the sidewall curvature. Hence, we consider three channels of rectangular cross-section and dimensionless thickness $\epsilon = 1$, in which two straight portions are connected by a curved section, such that the left sidewall can be described by an analytical function $f(x)$. Figure 12 shows a top view of the

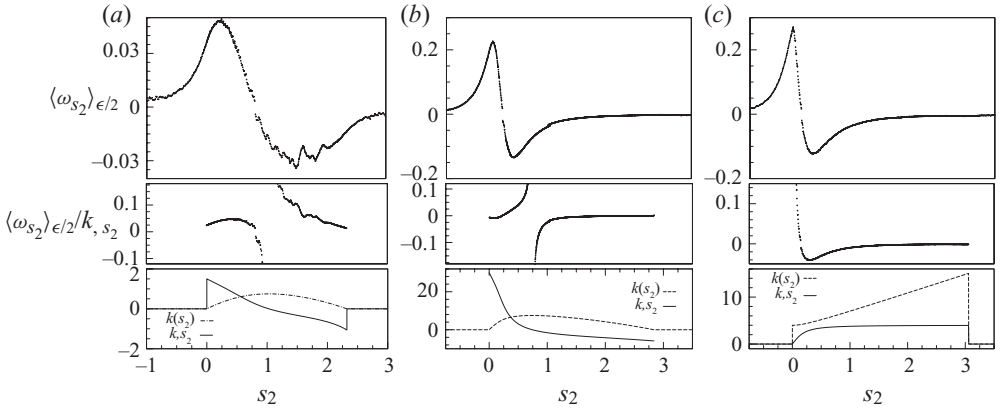

FIGURE 13. For the three channels shown in figure 12, from top to bottom: component of the vorticity along s_2 at the left sidewall of the channel, averaged over half the channel thickness, versus the streamwise coordinate s_2; ratio between the defined quantity $\langle\omega_{s_2}\rangle_{\epsilon/2}$ and the derivative of the wall curvature $k_{,s_2}$; for the left sidewall, curvature $k(s_2)$ and derivative of curvature $k_{,s_2}$ versus the streamwise coordinate s_2.

contour plot of the component of velocity orthogonal to the plane of the channel u_z in a plane located at $z = 3/4$. For the geometries in figure 12(*a*,*b*) $f(x)$ in the curved part is given by two fourth-order polynomial functions, only differing by a constant factor, with both the first and the second derivatives continuous at the two ends of the curved part. For the geometry in figure 12(*c*), $f(x)$ is instead an hyperbolic cosine. For the three geometries a secondary flow, characterized by two regions of opposite sign vorticity of different intensity, is present along both sidewalls.

In the context of Balsa's approach, we discuss the variation of geometric and fluid-dynamic quantities along the curvilinear coordinate s_2. Figure 13 compares, for the geometries in figure 12, the behaviours along the curvilinear coordinate s_2 of the streamwise vorticity at the wall ω_{s_2}, averaged over half the channel thickness, of the sidewall curvature $k(s_2)$ and of its derivative $k_{,s_2}$. Figure 12 also shows the ratios of the streamwise vorticity and of the corresponding derivative of the curvature of the side boundary along the coordinate s_2. We observe: (i) for geometries (figure 12*a*,*b*) the derivative of the curvature $k_{,s_2}$ has a sawtooth shape, which is mimicked, even if slightly anticipated, by the streamwise vorticity distribution at the wall; (ii) this agreement is stronger for geometry (figure 12*a*), which is characterized by smaller values of $k_{,s_2}$, hence by a slower change in curvature (we note that the ratio $\langle\omega_{s_2}\rangle_{\epsilon/2}/k_{,s_2}$ is positive over most of the curved region); (iii) for geometry (figure 12*c*) the derivative of the curvature is not defined at the extrema of the curved section and these discontinuities lead to peaks in the secondary vorticity profile. Comparing the three results, we see that the wall vorticity does not scale linearly with the rate of change of the curvature of the side boundary. This is in agreement with the observation for the case of rounded turns with different radii of curvature (see § 5.2), i.e. the maximum vorticity at the wall is proportional to the change in curvature of the boundary only over a certain range of radii of curvature, while its value tends to saturate when R is further reduced.

As a last example, we evaluate a pressure-driven flow in a channel, where a rectilinear section evolves in a spiral-like shape. Also, in this case the channel cross-section remains constant and characterized by $\epsilon = 1$. Figure 14(*a*) provides contour plots of the component of the velocity field orthogonal to the plane of the channel u_z

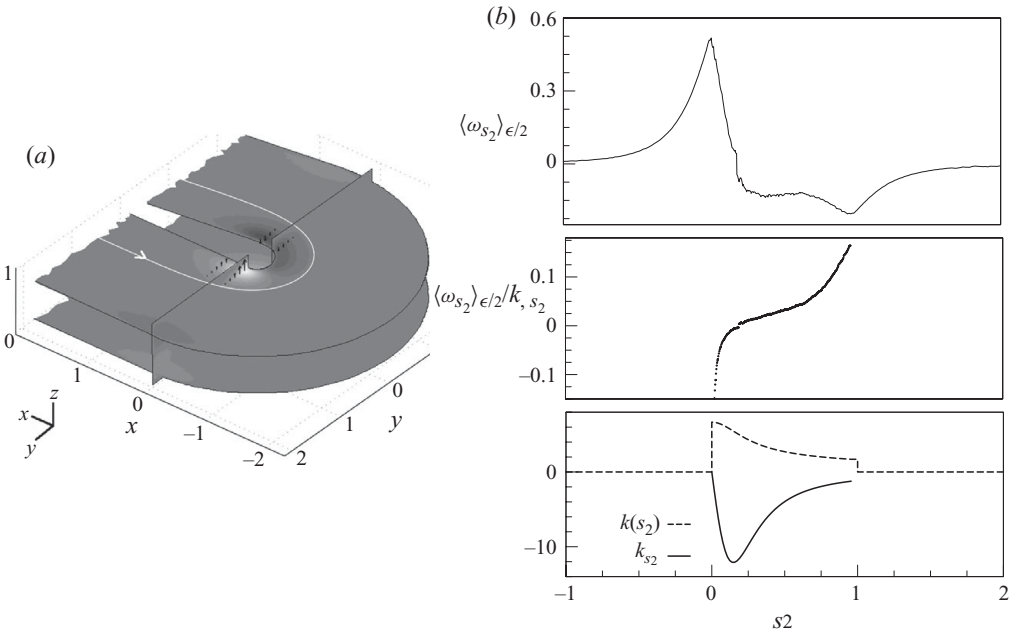

FIGURE 14. Pressure-driven flow in a channel with rectangular cross-section of dimensionless thickness $\epsilon = 1$ and characterized by a rectilinear section which evolves in a spiral-like shape, described by the parametric expressions $(x(\theta) = -0.3\theta\cos\theta,\ y(\theta) = -0.3\theta\sin\theta)$. $Re = 0.001$. (*a*) Contour plots of the component of velocity orthogonal to the plane of the channel u_z on two planes at constant z and in two cross-sectional planes are shown. White, black and grey contours represent, respectively, positive, negative and vanishing values of u_z. A streamline is added to suggest the direction of the flow. (*b*) From top to bottom: component of the vorticity along s_2 at the left sidewall of the channel, averaged over half the channel thickness, versus the curvilinear coordinate s_2; ratio between the quantity $\langle\omega_{s_2}\rangle_{\epsilon/2}$ and the derivative of the sidewall curvature $k_{,s_2}$; for the left sidewall, curvature $k(s_2)$ and derivative of curvature $k_{,s_2}$ versus the streamwise curvilinear coordinate s_2.

at planes $z = \{1/4, 3/4\}$ and in two cross-sections, in order to visualize the extension and the sign of the secondary flow. Such a three-dimensional velocity distribution gives rise at the sidewall to the streamwise vorticity distribution in figure 14(*b*, top). We note a strong vorticity peak at the beginning of the curved section, a subsequent opposite sign vorticity distribution along the development of the spiral, and a last peak, where the spiral-like section blends into a straight section. Figure 14(*b*) also shows the sidewall curvature $k(s_2)$, its rate of change $k_{,s_2}$, and the ratio between the average wall vorticity and $k_{,s_2}$, as function of the curvilinear streamwise coordinate s_2. We observe: (i) the two positive and negative peaks of vorticity identified are due to the discontinuity in the wall curvature at the two ends of the spiral-like shape section; (ii) in the central part of the curved section, where the curvature changes smoothly, ω_{s_2} has the same sign as $k_{,s_2}$ and the ratio between these two quantities tends to change only slowly.

Based on these results, we suggest that, even if locally, along a wall whose curvature changes smoothly, the intensity of the secondary flow is related to the derivative of the curvature, there is nevertheless a significant non-local effect. In fact, given the viscous nature of the phenomenon, the flow field far from the boundary knows about the variation at the boundary and the streamlines bend accordingly, thus generating a

cross-stream flow, which induces the secondary flow near the wall. We thus generally expect non-local contributions to streamwise vorticity from the boundary shape.

6. Conclusions

We have shown that a low-Reynolds-number pressure-driven flow in a three-dimensional confined corner geometry exhibits well-defined three-dimensional flow features. We discussed in detail the case of a rectangular cross-section channel that is characterized by 90° turns. In cross-sectional planes located right before and after the turn, pairs of counter-rotating vortical structures are present, which we refer to as streamwise, or open, vortices, since the streamlines have a helical character. In other words, in a pressure-driven flow between two plane walls and around sidewalls that form a 270° corner in the fluid domain, the weak secondary flow is characterized by a single vortex per corner formed by the sidewall with the top or bottom wall. Such vortices are characterized by streamwise vorticity and helicity of alternating sign in the streamwise direction and in the direction orthogonal to the 270° angle. This result is in agreement with and complements the results obtained by Balsa (1998), Lauga *et al.* (2004), Shankar (2000), Gomilko *et al.* (2003). We have also shown that the basic vortical flow about the corner is inherently a viscous, zero-Reynolds-number phenomenon.

With reference to this corner geometry, we introduced a matched asymptotic expansion solution for the flow around two boundaries intersecting at an angle α and spanning the small gap between two horizontal plates. This approach provided a solution for the three-dimensional flow field in the boundary layer that develops along the sidewalls, approaching and leaving the corner, with the exception of the most inner region around the corner (figure 6). The analytical solution compares well with the full numerical solution for a pressure-driven flow in a finite channel, up to a cross-section aspect ratio $\epsilon \approx 1$.

For the case of a channel with a sharp 90° turn, we systematically varied the thickness of a channel of constant width, thus varying its aspect ratio, and demonstrated that, over a range of the dimensionless thickness ($\epsilon \leqslant 2$), the most significant dimension in the description of the secondary flow is the channel thickness. When the channel thickness is larger than the width, then also the latter becomes relevant to determine the secondary flow. Also, in general, the magnitude of the streamwise vorticity at the wall decreases monotonically as the radius R of the 90° turn is increased. Finally, we considered channel geometries such that the curvature of the side boundary changed continuously: the strength of the vorticity associated with the secondary flow is determined by the rate of change of the curvature of the boundary.

As explained in § 1, our work was inspired by a recent experiment that showed the formation of 'thread-like' biofilms in microchannels, hence in low-Reynolds-number conditions, whenever the geometry has corners. On-going work is focused on demonstrating the relationship between the formation of streamers and an underlying hydrodynamic mechanism related to the viscous secondary flow. Such vortical structures, even if characterized by very weak velocities, might have an effect on local mass or heat transport when long time scales are involved.

We thank H. Bau, A. Forsyth, U. Hees, J. Hinch, R. Kolter, R. Losick, J. Rieger, B. Scheid, B. Sobotka and S. Weinbaum for helpful discussions, and the

BASF-Harvard working group for the useful feedback. This work was supported by the BASF Advanced Research Initiative at Harvard University.

Appendix. Details of the boundary layer description

Some of the results reported here follow the formalism introduced by Balsa (1998). For completeness, we list here the leading-order momentum and continuity equations for the inner region, which have already been summarized in (4.7)

$$\frac{\partial \hat{p}^{(0)}}{\partial \hat{x}} = \nabla_{\perp}^2 \hat{u}_x^{(0)}, \tag{A 1a}$$

$$\frac{\partial \hat{p}^{(0)}}{\partial \hat{y}} = 0, \tag{A 1b}$$

$$\frac{\partial \hat{p}^{(0)}}{\partial \hat{z}} = 0. \tag{A 1c}$$

$$\frac{\partial \hat{p}^{(1)}}{\partial \hat{x}} = \nabla_{\perp}^2 \hat{u}_x^{(1)}, \tag{A 2a}$$

$$\frac{\partial \hat{p}^{(1)}}{\partial \hat{y}} = 0, \tag{A 2b}$$

$$\frac{\partial \hat{p}^{(1)}}{\partial \hat{z}} = 0. \tag{A 2c}$$

$$\nabla_{\perp}^2 \hat{\boldsymbol{u}}_{\perp}^{(0)} = \nabla_{\perp} \hat{p}^{(2)}, \tag{A 3a}$$

$$\frac{\partial \hat{u}_x^{(0)}}{\partial \hat{x}} + \nabla_{\perp} \cdot \hat{\boldsymbol{u}}_{\perp}^{(0)} = 0. \tag{A 3b}$$

We also show how the matching condition, expressed finally in inner variables, for the pressure in the inner region as $\hat{y} \to \infty$ is evaluated

$$\begin{aligned} \hat{p}_{\infty} &= p^{(0)}(\hat{x}, 0) + \delta \hat{y} \left.\frac{\partial\, p^{(0)}}{\partial y}\right|_{\hat{x},0} + \left.\frac{(\delta \hat{y})^2}{2} \frac{\partial^2 p^{(0)}}{\partial y^2}\right|_{\hat{x},0} \\ &\quad + \delta \left(p^{(1)}(\hat{x}, 0) + \delta \hat{y} \left.\frac{\partial\, p^{(1)}}{\partial y}\right|_{\hat{x},0} + \cdots \right) + \cdots \\ &= p^{I(0)}(\hat{x}) + \delta\, p^{I(1)}(\hat{x}) + \delta^2\, p^{I(2)}(\hat{x}, \hat{y}) + \ldots, \end{aligned} \tag{A 4}$$

where we know that, for the outer pressure given in (4.4), $\partial\, p^{(0)}/\partial y|_{\hat{x},0} = 0$. After some manipulations, (A 4) and (4.4) provide

$$p^{I(0)}(\hat{x}) = p^{(0)}(\hat{x}, 0), \tag{A 5a}$$

$$p^{I(1)}(\hat{x}) = p^{(1)}(\hat{x}, 0), \tag{A 5b}$$

$$p^{I(2)}(\hat{x}) = \left.\frac{\hat{y}^2}{2} \frac{\partial^2 p^{(0)}}{\partial y^2}\right|_{\hat{x},0} + \hat{y} \left.\frac{\partial p^{(1)}}{\partial y}\right|_{\hat{x},0} = -\frac{\hat{y}^2}{2} \frac{d^2 p^{I(0)}}{d\, \hat{x}^2} + \hat{y} \left.\frac{\partial p^{(1)}}{\partial y}\right|_{\hat{x},0}. \tag{A 5c}$$

Since from the momentum equation we have (A 1*b*), using the matching condition (A 5*a*) we can write for the component of velocity along $\hat{x}$ the problem given by (4.9) and the homogeneous boundary conditions at the walls $\hat{u}_x^{(0)}(\hat{x}, \hat{y} = 0, \hat{z}) = 0$, $\hat{u}_x^{(0)}(\hat{x}, \hat{y}, \hat{z} = \pm 1) = 0$. We look for a solution of the form (4.12*a*), with $\nabla_x^2 f(\hat{y}, \hat{z}) = 1$,

and obtain, via a Fourier-series expansion

$$\hat{u}_x^{(0)}(\hat{x},\hat{y},\hat{z}) = -\frac{4}{\pi^3}\frac{\mathrm{d}\,p^{I(0)}}{\mathrm{d}\,\hat{x}}\mathscr{B}(\hat{y},\hat{z}), \quad \mathscr{B}(\hat{y},\hat{z}) = \sum_{n=1,3,5,\ldots}^{\infty}\frac{\sin n\pi\hat{z}}{n^3}(1-\mathrm{e}^{-n\pi\hat{y}}). \tag{A 6}$$

The matching condition for the inner pressure field given in (A 5*c*) allows to say that, in the limit for $\hat{y}\to\infty$, $\hat{u}_z^{(0)}\to 0 = \hat{u}_{z\infty}^{(0)}$, and

$$\hat{u}_y^{(0)}(\hat{x},\hat{y},\hat{z}) \to \frac{4}{\pi^3}\frac{\mathrm{d}^2 p^{I(0)}}{\mathrm{d}\,\hat{x}^2}\sum_{n=1,3,5.}^{\infty}\frac{\sin n\pi\hat{z}}{n^3}\hat{y} - \frac{4}{\pi^3}\left.\frac{\partial p^{(1)}}{\partial y}\right|_{\hat{x},0}\mathscr{B}(\hat{y},\hat{z}) = \hat{u}_{y\infty}^{(0)}. \tag{A 7}$$

The continuity (4.7*c*), introduced the definitions (4.10*b*), becomes

$$\begin{aligned}\frac{\partial\hat{u}_y^*}{\partial\hat{y}} + \frac{\partial\hat{u}_z^*}{\partial\hat{z}} &= -\frac{\partial\hat{u}_x^{(0)}}{\partial\hat{x}} - \frac{\partial\hat{u}_{y\infty}^{(0)}}{\partial\hat{y}}\\ &= \frac{4}{\pi^3}\frac{\mathrm{d}^2 p^{I(0)}}{\partial\hat{x}^2}\mathscr{B} - \frac{4}{\pi^3}\frac{\mathrm{d}^2 p^{I(0)}}{\mathrm{d}\,\hat{x}^2}\sum_{n=1,3,5.}^{\infty}\frac{\sin n\pi\hat{z}}{n^3} + \frac{4}{\pi^3}\left.\frac{\partial p^{(1)}}{\partial y}\right|_{\hat{x},0}\sum_{n=1,3,5,\ldots}^{\infty}\frac{\sin n\pi\hat{z}}{n^2}\pi\mathrm{e}^{-n\pi\hat{y}}\\ &= -\frac{4}{\pi^3}\frac{\mathrm{d}^2 p^{I(0)}}{\mathrm{d}\,\hat{x}^2}\sum_{n=1,3,\ldots}^{\infty}\frac{\sin n\pi\hat{z}}{n^3}\mathrm{e}^{-n\pi\hat{y}} + \frac{4}{\pi^3}\left.\frac{\partial p^{(1)}}{\partial y}\right|_{\hat{x},0}\sum_{n=1,3,\ldots}^{\infty}\frac{\sin n\pi\hat{z}}{n^2}\pi\mathrm{e}^{-n\pi\hat{y}}. \end{aligned}\tag{A 8}$$

If we require that the integral over a cross-section of the right-hand side of (A 8) vanishes, we obtain the condition

$$\left.\frac{\partial p^{(1)}}{\partial y}\right|_{\hat{x},0} = \frac{\mathrm{d}^2 p^{I(0)}}{\mathrm{d}\,\hat{x}^2}\frac{\gamma}{\pi}, \quad \gamma = \sum_{n=1,3,5,\ldots}^{\infty}\frac{1}{n^5}\Bigg/\sum_{n=1,3,5.}^{\infty}\frac{1}{n^4}\approx 0.989993, \tag{A 9}$$

which when substituted into (A 8) yields:

$$\frac{\partial\hat{u}_y^*}{\partial\hat{y}} + \frac{\partial\hat{u}_z^*}{\partial\hat{z}} = -\frac{\mathrm{d}^2 p^{I(0)}}{\mathrm{d}\,\hat{x}^2}\sum_{n=1,3,5,\ldots}^{\infty}A_n\sin n\pi\hat{z}\,\mathrm{e}^{-n\pi\hat{y}}, \quad A_n = \frac{4}{\pi^3}\left(\frac{1}{n^3}-\frac{\gamma}{n^2}\right). \tag{A 10}$$

At this point, the problem is identical to the mathematical question addressed in Balsa (1998, starting with equation (30). It is convenient to introduce the vector function $\boldsymbol{f}_\perp(\hat{y},\hat{z})$, thus seeking a solution of the secondary flow $\hat{\boldsymbol{u}}_\perp^*$ of the form of (4.12*b*). Balsa (1998) proceeds by writing $\boldsymbol{f}_\perp(\hat{y},\hat{z})$ in terms of a velocity potential $\phi(\hat{y},\hat{z})$ and a stream-function $\psi(\hat{y},\hat{z})$, which is used to satisfy the boundary conditions at the walls. The solutions for ϕ and ψ have the form of Fourier series in $\hat{y}$ and exponential and Green functions in $\hat{z}$ (Balsa 1998). From these details, we deduce $\hat{u}_z\propto\exp(-2\pi\hat{y})$ as $\hat{y}\to\infty$, which was compared with numerical results in the main body of the paper.

REFERENCES

Balsa, T. F. 1998 Secondary flow in a Hele-Shaw cell. *J. Fluid Mech.* **372**, 25–44.

Davis, A. M. J. & O'Neill, M. E. 1977 Separation in a slow linear shear flow past a cylinder and a plane. *J. Fluid Mech.* **81**, 551–564.

Gomilko, A. M., Malyuga, V. S. & Meleshko, V. V. 2003 On steady Stokes flow in a trihedral rectangular corner. *J. Fluid Mech.* **476**, 159–177.

Hills, C. P. & Moffatt, H. K. 2000 Rotary honing: a variant of the Taylor paintscraper problem. *J. Fluid Mech.* **418**, 119–135.

Jeffrey, D. J. & Sherwood, J. D. 1980 Streamline patterns and eddies in low-Reynolds-number flow. *J. Fluid Mech.* **96**, 315–334.

Lauga, E., Stroock, A. D. & Stone, H. A. 2004 Three-dimensional flows in slowly varying planar geometries. *Phys. Fluids* **16**, 3051–3062.

Lee, J. S. & Fung, Y. C. 1969 Stokes flow around a circular cylindrical post confined between two parallel plates. *J. Fluid Mech.* **37**, 657–670.

Liu, R. H., Stremler, M. A., Sharp, K. V., Olsen, M. G., Santiago, J. G., Adrian, R. J., Aref, H. & Beebe, D. J. 2000 Passive mixing in a three-dimensional serpentine microchannel. *J. Microelectromech. Syst*. **9**, 190–197.

Moffatt, H. K. 1964 Viscous and resistive eddies near a sharp corner. *J. Fluid Mech.* **18**, 1–18.

Riegels, F. 1938 Zur kritik des Hele-Shaw-versuchs. *ZAMM* **18**, 95–106.

Rusconi, R., Lecuyer, S., Guglielmini, L. & Stone, H. A. 2010 Laminar flow around corners triggers the formation of biofilm streamers. *J. R. Soc. Interf.* **7**, 1293–1299.

Shankar, N. P. 2000 On Stokes flow in a semi-infinite wedge. *J. Fluid Mech.* **422**, 69–90.

Shankar, P. N. 2007 *Slow Viscous Flow*. Imperial College Press.

Squires, T. M. & Quake, S. R. 2005 Microfluidics: fluid physics on the nanoliter scale. *Rev. Mod. Phys.* **77**, 977–1026.

Stone, H. A., Stroock, A. D. & Ajdari, A. 2004 Engineering flows in small devices. *Annu. Rev. Fluid Mech.* **36**, 381–411.

Thompson, B. W. 1968 Secondary flow in a Hele-Shaw cell. *J. Fluid Mech.* **31**, 379–395.

Yi, M. & Bau, H. H. 2003 The kinematics of bend-induced mixing in micro-conduits. *Intl J. Heat Fluid* **24**, 645–656.